

# Nanoengineered Skeleton-surface of Nickel Foam with Additional Dual Functions of Rate-capability Promotion and Cycling-life Stabilization for Nickel Sulfide Electrodes

Yanhong Li,<sup>[a, b]</sup> Yuanyuan Liu,<sup>[a]</sup> Jing Li,<sup>[a]</sup> Meiri Wang,<sup>[a]</sup> Wei Wang,<sup>\*[a]</sup> and Hongtao Cui<sup>\*[a]</sup>

**Abstract:** Battery-type electrode materials such as NiS applied in Faradaic supercapacitors (FSs) could display poor performance with regard to rate-capability and cycling stability due to the inappropriate texture of the electrodes. Numerous works focussed on tuning the microscopic structure of electrode materials, but neglected the influence of the microscopic structure of current collectors such as nickel foam on the electrochemical performance of FSs. In this work, the performance of NiS is associated with the micro-

scopic structure of nickel foams by decorating the 2D porous nanostructured NiS on a 2D nanoengineered skeleton-surface of nickel foams. It could be inferred from the characterization results that the synergistic effect of both 2D nanostructured NiS and nickel foam significantly promotes the rate-capability and stabilizes the performance of NiS. Asymmetric supercapacitors using the dually nanostructured NiS/nickel foam as positive electrode and AC as negative electrode exhibit both high energy and high power densities.

## Introduction

Supercapacitors (SCs) are one category of attracting energy storage devices for the application in some burgeoning areas such as portable electronics, hybrid electric vehicles, smart electricity grids storing the intermittent energy, etc.<sup>[1–7]</sup> The two basic types of SCs including electrical double layer capacitors (EDLCs) and Faraday supercapacitors (FSs) present their own featured electrochemical mechanisms of energy storage and release. The mechanism of electrostatic attraction at the carbon/electrolyte interface is the source of the high power density and low energy density signature of EDLCs,<sup>[8,9]</sup> and yet the mechanism of faradaic redox reaction of FSs leads to its converse signature.<sup>[10–13]</sup> Consequently, one prevailing research interests focuses on the construction of nanostructured electrodes in FSs, trying to achieve SCs with both high energy and high power densities.<sup>[14–17]</sup>

It is known that the capacitance of FSs arises from the faradaic redox reactions at/near the surface of a material in contact with electrolyte ions. Based on this electrochemical mechanism, there exist two strategies of assembling electrodes in FSs: (1) coating the nanostructured materials on current collectors by the traditional manufacturing method of electrodes; (2) decorating the nanostructured materials on the skeleton surface of current collectors. For the first strategy, the simple

coating of nanostructured materials on current collectors would induce the disordered packing of material particles in electrodes, thus resulting in the unsmooth transfer of electrolyte ions from electrolyte solution into electrodes. On the other hand, the using of binder for the coating process would significantly reduce the electrical conductivity of electrodes. For the second strategy, relevant works reveals that the electrodes in which the current collectors are decorated with structurally well-designed materials are highly favorable to the charge-discharge process, showing excellent electrochemical characteristics much superior to the electrodes assembled by coating the nanostructured materials on current collectors.<sup>[18–21]</sup> This stems from the fact that the electrodes with structurally well-designed materials decorated on current collectors fits the electrochemical mechanism of FSs, especially for the battery-type electrode materials. Based on these considerations, it could be concluded that the current collector is a key for the assembly of high-performance electrodes, which is responsible for the smooth transportation of electrons and also the electrochemical performance of electrode materials.

Some carbon materials such as carbon nanotubes, carbon foam, and carbon cloth are emerging as new types of current collectors due to their excellent electrical conductivity and suitable microstructure for the decoration of electro-active materials as compared with the traditional current collectors such as nickel foam.<sup>[22–24]</sup> However, these carbon materials have not become the predominant current collectors in FSs owing to their intrinsic disadvantages such as low mechanical strength, hydrophobicity, high cost, and difficulty in preparation.<sup>[25]</sup> The nickel foam with micron-scale 3D framework has been extensively used as current collector in batteries due to its appropriate electrical conductivity, mechanical strength, and alkali resistance. In the FSs using alkali as electrolyte, nickel foam has been considered as the optimum current collector precisely because of these advantages.

[a] Y. Li, Dr. Y. Liu, Dr. J. Li, Prof. M. Wang, Dr. W. Wang, Prof. H. Cui  
College of Chemistry and Chemical Engineering  
Yantai University  
264005 Yantai (China)  
E-mail: wangwei\_ytu@163.com  
htcui@ytu.edu.cn

[b] Y. Li  
Yantai Institute of Coastal Zone Research  
Chinese Academy of Sciences  
264005 Yantai (China)

Supporting information for this article is available on the WWW under <https://doi.org/10.1002/cnma.202000296>

Most of works have focused on decorating various hierarchical nanostructures of materials on the skeleton surface of nickel foam.<sup>[26–32]</sup> However, it is worth noting that almost no works cares about the effect of microstructure of nickel foam on the electrochemical performance of FSs. It is known that the most prominent weakness of nickel foam is the negligible surface area of its micron-scale framework. Therefore, to keep the high capacity of materials, the loading amount of materials on nickel foam is quite limited, which would result in the low energy density of FSs. To pursue high energy, the materials have to grow upwardly on the skeleton surface of nickel foam in order to load appreciable amount of materials. The issue arising therefrom is the low percentage of contact area between nickel foam and materials, which thus causes two consequences:<sup>[33–36]</sup> (1) the obstructed electron transportation between materials and current collector, especially for the weakly conductive materials such as sulfides, hydroxides, and most metal oxides, which would lead to the low rate-capability of materials and powder density of FSs; (2) the weak mechanical support for buffering the stress originating from the volume swelling and shrinking of electro-active materials during the charge-discharge cycles. In other words, the function of nickel foam is confined to the traditional role of current collector and the substrate for the decoration of nanostructured electrode materials. As a result, it is reasonable to infer that nano-engineering the skeleton surface of nickel foam to significantly increase its surface area and facilitate the growth of nanostructured materials is a key aspect for further boosting the performance of FSs.

Nickel sulfide is a promising battery-type electrode material for application in FSs due to its high theoretical specific capacity.<sup>[37–39]</sup> However, nickel sulfide also has the common weakness of transitional metal sulfides, namely the low electrical conductivity and low cycling stability. In this work, we tried to nanoengineer the skeleton surface of nickel foam by an electrodeposition method for its use as an advanced current collector with dual functions including electron transportation conductor and suitable carrier for the decoration of appreciable amount of nickel sulfide. During the electrodeposition, wrinkled nanostructure was produced on the skeleton surface of nickel foam, which thus increased the surface area of nickel foam. In the next step of electrodeposition, an appreciable amount of sheet-like nickel sulfide grew in a way fitting the wrinkled skeleton surface of nickel foam, forming a 2D porous wrinkled nanostructure. As a result of this ordered microstructure, the nickel sulfide electrode presented high rate-capability and enhanced cycling stability, which is attributed to the increased electrical conductivity of electrode, the thin thickness of wrinkles, and the fully functional mechanical support of nickel foam.

## Results and Discussion

The pristine nickel foam with 3D macroporous structure is an excellent current collector of FSs due to its above-mentioned advantages. The most significant disadvantage of nickel foam is

its negligible surface area, which is unfavorable to the electrochemical performance of FSs. In this work, we electrodeposited the nanostructured nickel sulfide on the pristine nickel foams and the skeleton surface-wrinkled nickel foams according to the scheme in Figure 1a, trying to associate the performance of FSs with the microstructure of current collector. The FE-SEM images in Figure 1b–c indicate that the skeleton of pristine nickel foam has the typical smooth surface. To create nanostructured surface, we treated the skeleton surface of pristine nickel foams by the chronopotentiometry electrodeposition method in an aqueous solution of  $\text{NiCl}_2$  and  $\text{NH}_4\text{Cl}$ . The FE-SEM images in Figure 1d–e show that the skeleton of as-electrodeposited nickel foam presents the homogeneously wrinkled surface. In the XRD patterns of Figure 1f–g, both the skeleton surface-wrinkled nickel foams and the powder falling from the nickel foams during the chronopotentiometry electrodeposition exhibit the typical structure of metal nickel (JCPDS no. 65-2865). The result of structural analysis proves that the wrinkled nanostructure on the skeleton surface of nickel foams is metal nickel. The formation mechanism of wrinkled nanostructure can refer to the two simultaneous processes mentioned in some works:<sup>[38,40,41]</sup> (1) the electrochemical reduction of nickel ions in nickel salt solution to form metal nickel; (2) the growth of metal nickel on the skeleton surface of nickel foam using the hydrogen bubbles produced via a water electrolysis reaction as dynamic template. The specific surface area of the skeleton surface-treated nickel foam calculated from its isotherms by the

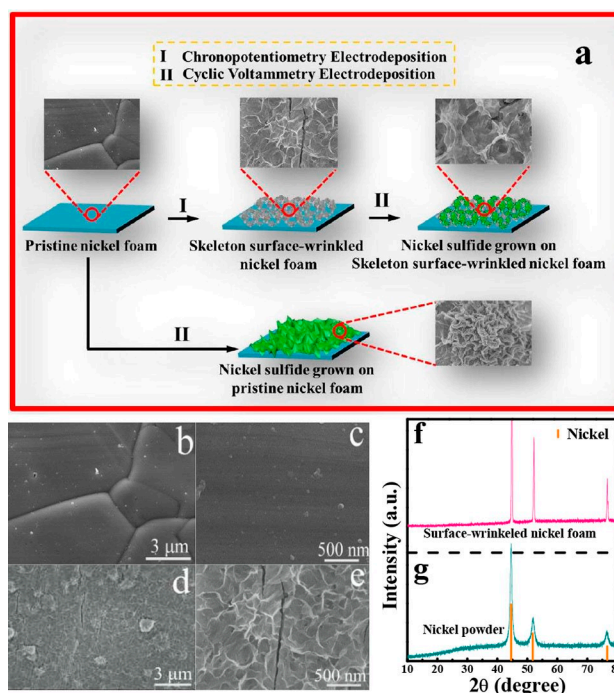


**Figure 1.** (a) Schematic illustration for the synthesis of nickel sulfide decorated on the pristine nickel foam and skeleton surface-wrinkled nickel foam; FE-SEM images of (b–c) pristine nickel foam and (d–e) skeleton surface-wrinkled nickel foam at different magnification; XRD patterns of (f) the skeleton surface-wrinkled nickel foam and (g) the nickel powder falling from nickel foam during the chronopotentiometry electrodeposition.

Brunauer-Emmett-Teller (BET) method is  $0.1694 \text{ m}^2 \text{ g}^{-1}$ , 4.3 times larger than that of pristine nickel foam ( $0.0395 \text{ m}^2 \text{ g}^{-1}$ ). This result indicates that the electrodeposition treatment can increase the specific surface area of nickel foam significantly by building the wrinkled nanostructure on the skeleton-surface.

According to the scheme in Figure 1a, the nickel sulfide was deposited on the pristine nickel foams (NF-x) and the skeleton surface-wrinkled nickel foams (ED-NF-x) by a cyclic voltammetry electrodeposition method at the respective scan rates of 5, 10, 15, 20 or  $25 \text{ mVs}^{-1}$ . Because the NF-x series samples exhibit the similar surface morphology, we just show the typical FE-SEM images of sample NF-15 in Figure 2a-b. The two images show that the nickel sulfide on the skeleton surface of NF-15 has the irregular distribution on the surface. In some locations of the surface, the nickel sulfide grows in a way fitting the smooth skeleton surface of nickel foam, forming a wrinkled 2D structure. In other locations, the nickel sulfide nanosheets are closely stacked together to form 3D clusters. In the FE-SEM images of Figure 2c-h, the ED-NF-x series samples then present the completely different morphology. These images reveal that these samples have much more homogeneous hierarchical nano-architecture of nickel sulfides on the skeleton surface than sample NF-15. It seems that the nickel sulfide nanosheets grow along the wrinkled skeleton surface of nickel foam, eventually forming the ordered 2D wrinkled nanostructure. The elemental mapping result in the inset of Figure 2 shows that the two elements of nickel and sulfur distribute in the nanostructure of nickel sulfide homogeneously. The FE-SEM images in Figure 2

also indicate that the difference between these ED-NF-x samples is the size, depth and pore wall thickness of macropores. It is observed that the size, depth and pore wall thickness decrease with the increase of scan rate. It looks that the pore structure almost disappears in the sample ED-NF-25, and its closely stacked nanosheet clusters look like those in sample NF-15. The  $\text{N}_2$  adsorption-desorption isotherms in Figure S1a indicates that the ED-NF-x series samples have a similar hysteresis loop suggesting their porous structure, while the sample NF-15 presents the type II isotherms referring to the less pore-structure. The calculated results from these isotherms show that the sample ED-NF-15 has the largest specific surface area of  $66.88 \text{ m}^2 \text{ g}^{-1}$  excluding the contribution of nickel foam substrate, much larger than that of sample NF-15 and other ED-NF-x series samples. Meanwhile, the pore size distribution curves in Figure S1b prove the richest mesopores in sample ED-NF-15. It could be inferred from these results of FE-SEM observation and surface analysis that the scan rate applied during the cyclic voltammetry electrodeposition has a significant influence on the morphology and surface area of the nickel sulfide decorated on the skeleton surface-wrinkled nickel foams.

We analyzed the elemental composition of the nickel sulfide powder samples (P-x) falling from the skeleton surface-wrinkled nickel foams during the cyclic voltammetry electrodeposition by various characterization methods including XRF, XPS and EDS. As shown in Table S1, the composition obtained by various characterization methods is approximately same for the same samples. Table 1 indicates that all samples have the nearly same composition with atomic ratio of 1:1 for the nickel and sulfur elements. The XRD patterns of ED-NF-x and P-x series samples in Figure S2 show that the nickel sulfide in these samples is amorphous. From these results, it could be concluded that the as-prepared nickel sulfide could be denoted as amorphous NiS. The XPS characterization result in Figure S3 shows that there exist both signals of  $\text{Ni}^{2+}$  ( $\text{Ni } 2\text{p}^{3/2} \sim 850.23 \text{ eV}$ ;  $\text{Ni } 2\text{p}^{1/2} \sim 867.43 \text{ eV}$ ) and  $\text{Ni}^{3+}$  ( $\text{Ni } 2\text{p}^{3/2} \sim 853.39 \text{ eV}$ ;  $\text{Ni } 2\text{p}^{1/2} \sim 871.31 \text{ eV}$ ) in these P-x series samples, confirming that the amorphous NiS is a multivalent nickel sulfide.

To associate the performance of NiS with the microstructure of current collector, we compare the electrochemical properties of the ED-NF-x series samples in Figure 3 and Figure S4 in the first step. In the CV curves (Figure 3a and Figure S4a), all these samples present a pair of redox peaks, corresponding to the typical faradaic behavior of nickel sulfide in alkaline electrolyte solution.<sup>[42,43]</sup> In the galvanostatic curves (Figure 3b and Figure S4b), the sample ED-NF-15 has the longest charge-discharge

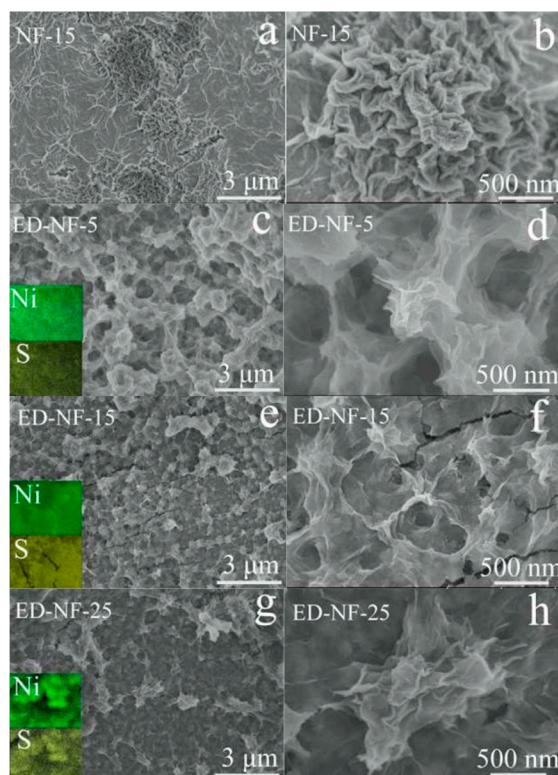


**Figure 2.** FE-SEM images of (a–b) NF-15, (c–d) ED-NF-5, (e–f) ED-NF-15, and (g–h) ED-NF-25; (insets) elemental mapping of nickel and sulfur.

Table 1. The reaction condition and sample no.			
Scan rate [ $\text{mV s}^{-1}$ ]	Nickel sulfide decorated on the skeleton surface-wrinkled nickel foams	Nickel sulfide powder	Nickel sulfide decorated on the pristine nickel foams
5	ED-NF-5	P-5	NF-5
10	ED-NF-10	P-10	NF-10
15	ED-NF-15	P-15	NF-15
20	ED-NF-20	P-20	NF-20
25	ED-NF-25	P-25	NF-25



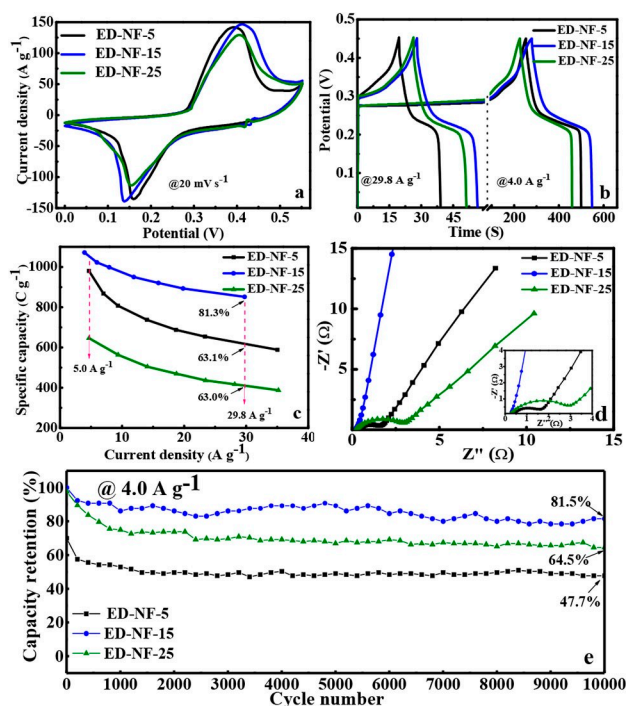


**Figure 3.** (a) CV curves at scan rate of  $20 \text{ mV s}^{-1}$ , (b) GCD curves, (c) curves of specific capacity vs. current density, (d) Nyquist plots, and (e) cycle stability of ED-NF-5, ED-NF-15, and ED-NF-25.

duration at low and high current densities. In the curves of specific capacity vs. current density (Figure 3c and Figure S4c), this sample exhibits the highest capacity within the whole range of current densities. It has the specific capacity of 1071, 1023, 998, 950, 921, 893 and  $851 \text{ Cg}^{-1}$  at the respective current densities of 4.0, 6.0, 7.9, 11.9, 15.9, 19.8 and  $29.8 \text{ A g}^{-1}$ . At a high current density of  $29.8 \text{ A g}^{-1}$ , its specific capacity still keeps 81.3% of the value at  $5.0 \text{ A g}^{-1}$ , while those of the samples ED-NF-5 and ED-NF-25 decay to 63.14% and 63.02%, respectively. This result demonstrates that the sample ED-NF-15 has much higher rate-capability than the other ED-NF-x series samples, which could be attributed to its lower interfacial charge-transfer resistance ( $R_{ct}$ ) originating from the smaller pore wall thickness of NiS. To prove this conclusion, we measured the electrochemical impedance spectroscopy (EIS) of these ED-NF-x samples. In the Nyquist plots derived from EIS (Figure 3d and Figure S4d), the almost vanished semicircle of sample ED-NF-15 demonstrate its lowest  $R_{ct}$ . This figure also shows that all the ED-NF-x series samples have almost same series resistance, which could be attributed to their similar ordered 2D wrinkled nanostructure growing along the surface of nickel foams. The cycling stability of the ED-NF-x series samples was tested to give a clue for understanding the relation between the structure and performance of NiS. The result in Figure 3e shows that the samples ED-NF-5, ED-NF-15, and ED-NF-25 have the respective capacity retentions of 69.9%, 92.3% and 89.5% after the initial 200 charge-discharge cycles. During the following cycles, the capacities of these three samples decay slowly. After 10000 cycles, these samples keep the 47.7%, 81.5%, and 64.5%

of their initial capacity respectively. In other words, the sample ED-NF-15 has the highest cycling stability. Based on the FE-SEM observation results, it could be inferred from the cycling stability test result in Figure 3e that the 2D structure with homogeneously distributed wrinkles is more favorable to buffer the stress generated in NiS during the electrochemical reaction.

In the second step to associate the performance of NiS with the microstructure of current collector, we compare the electrochemical properties of samples NF-15, ED-NF-15 and P-15 that were prepared at the exact same conditions. The results of electrochemical measurement in Figure 4 and Figure S5 could prove the key role of the microstructure of current collector in the electrochemical performance of NiS. In the CV (Figure 4a) and galvanostatic (Figure 4b) curves, the sample ED-NF-15 has the smallest redox potential difference ( $\Delta E$ ) (300, 270 and 320 mV for samples NF-15, ED-NF-15, and P-15, respectively), and the longest charge-discharge duration at low and high current densities. The smallest  $\Delta E$  of sample ED-NF-15 suggests its highest faradaic reaction reversibility. The curves of specific capacity vs. current density in Figure 4c indicate that the sample ED-NF-15 has the much higher rate-capability than the other two samples. To demonstrate the advantage of this sample, we compare it with the recently published works shown in Figure 4d. Because the nickel sulfide in most of literatures used specific capacitance ( $\text{F g}^{-1}$ ) as the capacity unit, we translated the specific capacity of NiS ( $\text{Cg}^{-1}$ ) in our work to

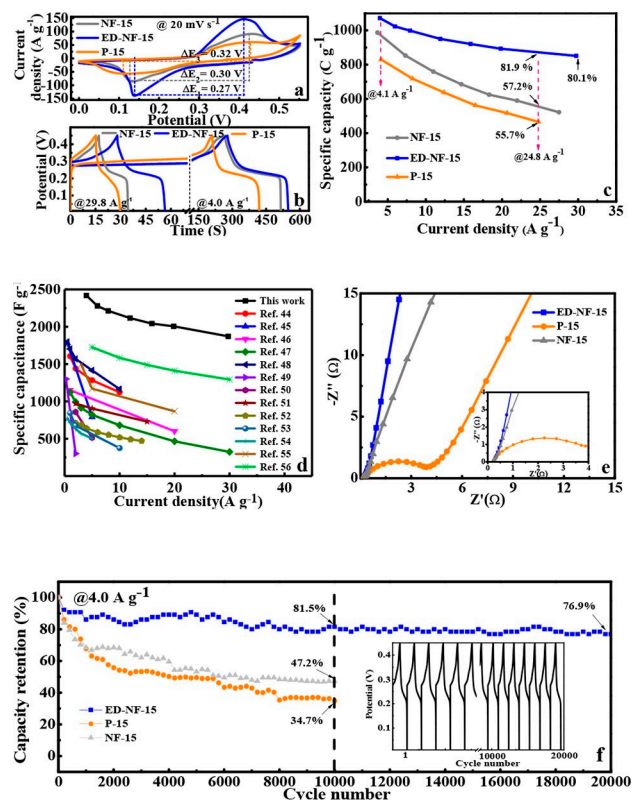


**Figure 4.** (a) CV curves at scan rate of  $20 \text{ mV s}^{-1}$ , (b) GCD curves, and (c) curves of specific capacity vs. current density for samples NF-15, ED-NF-15 and P-15; (d) Comparison of this work and other related works; (e) Nyquist plots and (f) cycling stability of samples NF-15, ED-NF-15 and P-15.

specific capacitance for the convenient comparison. In Figure 4d, it is shown that the sample ED-NF-15 has the highest electrochemical performance including specific capacitance and rate-capability among various nanostructured nickel sulfides.<sup>[44–54]</sup> It is noteworthy in the Nyquist plots of Figure 4e that the sample ED-NF-15 has the nearly same  $R_{ct}$  to NF-15, while it has much lower Warburg resistance ( $W$ ) than NF-15 (concluded from its larger slope). This EIS result is fully correspondent with the FE-SEM observation result in Figure 2. As shown in the FE-SEM images of Figure 2, both samples of NF-15 and ED-NF-15 present the similar 2D wrinkled structure with the similar thickness of wrinkles, which thus results in their nearly same  $R_{ct}$ . At the same time, the closely stacked NiS nanosheets clusters in the sample NF-15 would obstruct the fast transfer of electrolyte ions inside clusters, leading to its larger Warburg resistance than the sample ED-NF-15.

Based on the electrochemical principle of battery-type electrode materials in FSs, we can establish a relation between the cycling stability and structure of NiS. As shown in Figure 4f, the sample ED-NF-15 has much higher cycling stability than other two samples. It still remains 79.6% of its initial capacity after 20000 cycles, while the capacity of samples NF-15 and P-15 rapidly decays to 47.2% and 34.7% after 10000 cycles, respectively. In the FE-SEM images (Figure S6a–b), the sample

ED-NF-15 after 10000 cycles almost keeps its initial 2D wrinkled nanostructure on the surface of nickel foam, indicating its high structural stability. However, it is also observed that there exist some cracks in this sample, which may be the main reason for its decay of capacity. It is concluded from the results in Figure 4f and Figure S6 that the cycling stability of NiS is related with the interaction between NiS and current collector. The degree of mechanical supporting from current collector for these samples could be listed as ED-NF-15 > NF-15 > P-15. As a result, the cycling stability of these samples is correspondingly listed as the same sequence. This result agrees with the stabilizing mechanism of battery-type electrode materials in FSs.<sup>[22,33]</sup> Herein, it could be inferred from the above mentioned results that the synergistic effect of both nanostructured NiS and current collector has greater influence on the electrochemical performance of FSs than the unilateral nano-structuring.

In this work, we assembled the asymmetric supercapacitors (ED-NF-15//AC ASCs) shown in Figure 5a featuring both high energy and high power densities by employing the sample ED-NF-15 as positive electrode and activated carbon (AC) as negative electrode. Before testing the assembled ASCs, we measured the electrochemical properties of AC. As shown in Figure S7a, the CV curves of AC at different scan rates exhibits the characteristic electric double-layer capacitance within the

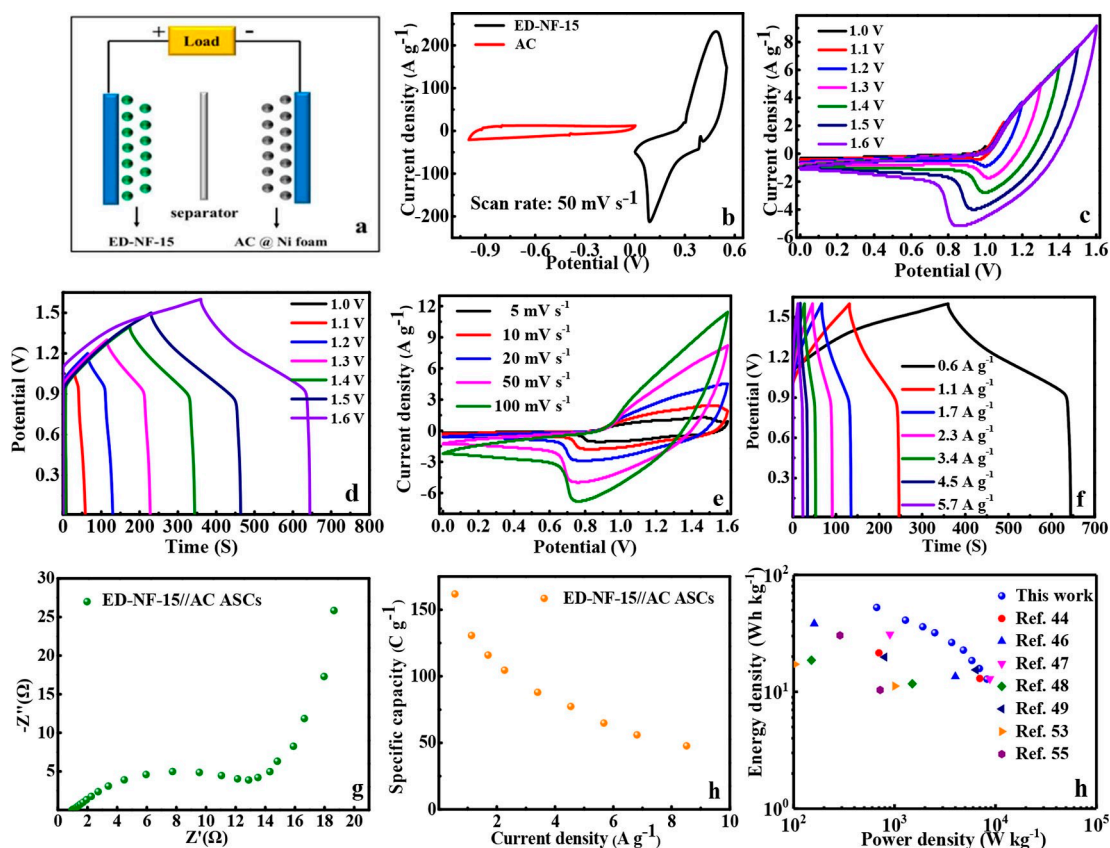


**Figure 5.** (a) Schematic illustration of ED-NF-15//AC ASCs; (b) CV curves of ED-NF-15 and AC at scan rate of  $50 \text{ mV s}^{-1}$ ; (c) CV curves and (d) GCD curves of ASCs with different cell voltages varying from 0–1 V to 0–1.6 V; (e) CV curves of ASCs at different scan rates; (f) GCD curves of ASCs at different current densities; (g) curve of specific capacity vs. current density for ASCs; (h) Nyquist plot of ASCs; (i) Ragone plot of ASCs and the comparison of this work with other related works (\* the two data points with the same color represent the respective energy densities at the corresponding high and low power densities).

potential range of  $-1.0-0$  V. The Figure S7b indicates that the AC has a high specific capacitance of  $267.0 \text{ Fg}^{-1}$  at  $2.6 \text{ Ag}^{-1}$ , which demonstrates that the AC can be used as a negative electrode in ASCs. In Figure 5b, the CV curves of sample ED-NF-15 and AC were respectively obtained at a scan rate of  $50 \text{ mVs}^{-1}$  in a three-electrode system. In this figure, the relatively ideal rectangular shape of CV curve for AC indicates its charge storage mechanism of electrical double layer capacitance, while the obvious redox peaks of CV curve for sample ED-NF-15 suggest the characteristics of its redox reactions. In Figure 5c–d, the CV and GCD curves of ASCs were measured in a  $3.0 \text{ M KOH}$  solution with different cell voltages varying from  $0-1 \text{ V}$  to  $0-1.6 \text{ V}$ . It could be judged from this figure that the optimal operating potential of ASCs is  $1.6 \text{ V}$  because there exists no obvious polarization phenomenon.

In Figure 5e, the CV curves of ASCs at scan rates from  $5$  to  $100 \text{ mVs}^{-1}$  demonstrate that the as-fabricated asymmetric supercapacitor has an excellent capacitive behavior within potential range of  $0-1.6 \text{ V}$ . The typical GCD curves at different current densities in Figure 5f show that the potential-time curves are almost symmetric at all current densities. The Nyquist plot in Figure 5g shows that the ASCs has a low series resistance ( $R_{\text{st}} = 0.97 \Omega$ ). The curve in Figure 5h indicates that the specific capacity of ASCs calculated from its GCD curves at different current densities show a high value of  $161.8 \text{ Cg}^{-1}$  at a low current density of  $0.6 \text{ Ag}^{-1}$ , and still keeps a high value of  $64.8 \text{ Cg}^{-1}$  at the high current density of  $5.7 \text{ Ag}^{-1}$ . In Figure 5i, the Ragone plot shows that the ASCs has an energy density of  $52.7 \text{ Whkg}^{-1}$  at the low power density of  $665.5 \text{ Wkg}^{-1}$ , and it keeps the energy density of  $18.5 \text{ Wkg}^{-1}$  at the high power density of  $5.8 \text{ kWkg}^{-1}$ . In this figure, we also compare the ED-NF-15//AC ASCs with those fabricated in other recently published works. It could be concluded from this figure that the ED-NF-15//AC ASCs has the highest energy density.

## Conclusion

In summary, NiS was decorated on the skeleton surface of nickel foams by a cyclic voltammetry electrodeposition method, forming a 2D wrinkled porous nanostructure of NiS fitting the wrinkled skeleton surface of nickel foams. The nanostructured nickel foam functions as an electrically conductive current collector and a suitable substrate for the 2D growth of nanostructured NiS. Based on the comprehensive results of characterization and electrochemical measurements, we could clarify the synergistic effect of both nanostructured NiS and current collector on the electrochemical performance of FSs. The 2D nanostructured NiS decorated on the 2D nanostructured skeleton-surface of nickel foams is beneficial for the transfer of electrolyte ions and electrons, thus favoring the faradaic reaction of NiS. As a result, the NiS presented a high rate-capability. On the other hand, the intimate contact between NiS and nickel foam is highly beneficial to the stress buffering of NiS during the charge-discharge cycles, thus resulting in an enhance cycling stability of NiS. Taken together, the results confirm that the structure synergistic effect of electrode

materials and current collector should be a focus in the area of FSs.

## Experimental Section

### Materials

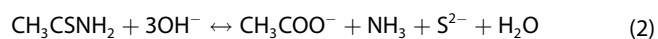
The analytical grade reagents used in the preparation were purchased from Aladdin, including ammonium chloride ( $\text{NH}_4\text{Cl}$ ), nickel nitrate hexahydrate ( $\text{Ni}(\text{NO}_3)_2 \cdot 6\text{H}_2\text{O}$ ,  $\geq 98\%$ ), nickel chloride ( $\text{NiCl}_2 \cdot 6\text{H}_2\text{O}$ ,  $\geq 99.0\%$ ), and thioacetamide ( $\text{C}_2\text{H}_5\text{NS}$ ,  $\geq 99.0\%$ ). The activated carbon used for the assembly of asymmetrical supercapacitors was purchased from XFANO, which has a specific surface area of  $2000 \pm 100 \text{ m}^2\text{g}^{-1}$ .

### Preparation of skeleton surface-wrinkled nickel foams

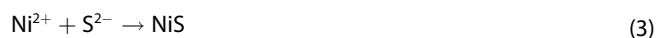
The skeleton surface-wrinkled nickel foams were prepared by an electrochemical deposition method using an IVIUMSTAT electrochemical workstation. The main specifications of electrochemical workstation is as following: current compliance  $\pm 5 \text{ A}$ ; maximum output voltage  $\pm 10 \text{ V}$ ; minimum current resolution  $0.6\text{mA}$ ; minimum potential resolution  $0.15 \text{ nV}$ ; frequency range  $10 \mu\text{Hz}$  to  $8 \text{ MHz}$ . Prior to the electrodeposition operation, the  $1.0 \times 1.0 \times 0.15 \text{ cm}$  sheet-like pristine nickel foams were cleaned with acetone, etched with  $6.0 \text{ M}$  hydrochloric, washed thoroughly with deionized water, and then dried in a vacuum oven at  $60^\circ\text{C}$  for  $6 \text{ h}$ . The two pretreated nickel foams were used as anode and cathode, respectively. The distance between the two electrodes was kept at  $1.0 \text{ cm}$  during the electrodeposition. The electrodeposition was carried out at a current density of  $2.5 \text{ A cm}^{-2}$  for  $60 \text{ s}$  in a  $20 \text{ mL}$  aqueous solution containing  $0.2 \text{ M NiCl}_2$  and  $4.5 \text{ M NH}_4\text{Cl}$ . After electrodeposition, the as-prepared skeleton surface-wrinkled nickel foams were washed with deionized water and ethanol for several times, and then dried in a vacuum oven at  $60^\circ\text{C}$  for  $6 \text{ h}$ .

### Decoration of nanostructured nickel sulfide on the skeleton surface-wrinkled nickel foams

A three-electrode cell was used to electrodeposit the nanostructured nickel sulfide on the skeleton surface-wrinkled nickel foams. A  $1.0 \times 1.0 \times 0.15 \text{ cm}$  skeleton surface-wrinkled nickel foam was used as a working electrode, a pristine nickel foam was used as a counter electrode, and an Ag/AgCl electrode was used as a reference electrode. The electrodeposition was carried out with the above-mentioned electrochemical workstation in a  $20 \text{ mL}$  aqueous solution containing  $4.0 \text{ mM Ni}(\text{NO}_3)_2$  and  $0.04 \text{ M}$  thioacetamide by cyclic voltammetry technique at the respective scan rates of  $5, 10, 15, 20$  or  $25 \text{ mVs}^{-1}$  for  $15 \text{ min}$  within a potential window of  $-1.2$  to  $0.2 \text{ V vs. Ag/AgCl}$ . As shown in equation 1, the water was electrolyzed to produce  $\text{H}_2$  and  $\text{OH}^-$  ions. The thioacetamide in the alkaline environment around working electrode was hydrolyzed to form  $\text{S}^{2-}$  ions (equation 2)). At the same time, the  $\text{Ni}^{2+}$  ions reacted with  $\text{S}^{2-}$  ions to produce NiS (equation 3). The obtained nickel sulfide-deposited nickel foam was washed by deionized water and ethanol, and subsequently dried in a vacuum oven at  $60^\circ\text{C}$  for  $12 \text{ h}$ . These as-obtained samples are denoted as the series of ED-NF-x as shown in Table 1.







At the same time, the black powder falling off from the ED-NF-x nickel foam during the electrodeposition was collected and rinsed with deionized water and ethanol and subsequently dried in a vacuum oven at 60 °C for 12 h. These samples are denoted as the series of P-x (Table 1). To investigate the influence of nickel foam pretreatment, the nickel sulfide was also electrodeposited on the 1.0×1.0×0.15 cm sheet-like pristine nickel foams at the exactly same preparation conditions to that of sample series of ED-NF-x. The obtained samples are denoted as the series of NF-x (Table 1).

### Characterization

The crystallographic structure and N<sub>2</sub> adsorption/desorption isotherms of samples were characterized by a Rigaku SmartLab III diffractometer (XRD) using Cu K $\alpha$  radiation ( $\lambda = 1.5406 \text{ \AA}$ ) and an ASAP-2010 surface area analyzer, respectively. The morphology of samples was observed by a JEOL JEM-1400 transmission electron microscope (TEM) and a Hitachi S-8010 cold-cathode field-emission scanning electron microscope (FE-SEM), respectively. The composition of samples was analyzed by a Rigaku Supermini 200 X-ray fluorescence spectrometer (XRF). The energy dispersive spectroscopy (EDS) of samples was measured by an Oxford Ultim Extreme detector. The X-ray photoelectron spectroscopy (XPS) analysis on the samples was carried out with a ESCALAB Xi+ X-ray photoelectron spectrometer.

### Electrochemical measurements

The electrochemical measurements on the electrode material were carried out in a 3.0 M KOH aqueous solution with an IVIUMSTAT electrochemical workstation in a three-electrode cell equipped with a working electrode, a platinum plate counter electrode, and an Hg/HgO reference electrode. The samples of ED-NF-x and NF-x were directly used as the working electrodes (containing ~2.5 mg nickel sulfide). The working electrodes for the P-x powder samples (containing ~2.5 mg nickel sulfide) were prepared according to the following procedure: an ethanol-wetted homogeneous mixture of P-x powder (80 wt%) and acetylene black (20 wt%) was ground to a paste and compressed at 10 MPa for 5 min onto a 1.0×1.0×0.15 cm sheet-like pristine nickel foam with a nickel wire for electrical connection; then, the coated nickel foam was dried at room temperature. The electrochemical measurements included cyclic voltammetry (CV), galvanostatic charge-discharge (GCD), and electrochemical impedance spectroscopy (EIS). The cycling life of materials was tested by a LANHE CT2001 A batteries testing system in the above mentioned three-electrode cell. Before measurements, the working electrodes were electro-activated in a 3.0 M KOH aqueous solution through 100 CV cycles at the scan rate of 100 mV s<sup>-1</sup>.

The specific capacity of nickel sulfide (C g<sup>-1</sup>) in three-electrode configuration was calculated from its discharge curves according to equation 4.<sup>153,54)</sup>

$$C_+ = \frac{i^* \Delta t}{m} \quad (4)$$

where C<sub>+</sub> is the specific capacity (C g<sup>-1</sup>), i is the discharge current (A),  $\Delta t$  is the discharge time (s), and m is the mass (g) of active material in electrodes, respectively.

The specific capacitance (F g<sup>-1</sup>) of activated carbon (AC) in three-electrode configuration was calculated from its discharge curves by equation 5:

$$C_- = \frac{i^* \Delta t}{m^* \Delta V} \quad (5)$$

where C<sub>-</sub> is the specific capacitance (F g<sup>-1</sup>), i is the discharge current (A),  $\Delta t$  is the discharge time (s), and m is the mass (g) of AC in the electrode,  $\Delta V$  (V) is the potential range of negative electrode during the charge-discharge process, respectively.

The asymmetrical supercapacitors (ASCs) were assembled using ED-NF-x as positive electrode, AC as negative electrode, and 3.0 M KOH aqueous solution as electrolyte. The negative electrodes were prepared by coating AC onto the 1.0×1.0×0.15 cm sheet-like pristine nickel foam under compression at 10 MPa. The mass of positive and negative electrodes was balanced according to equation 6:

$$\frac{m_+}{m_-} = \frac{C_- \Delta V}{C_+} \quad (6)$$

where C<sub>+</sub> is the specific capacity of positive electrode, C<sub>-</sub> is the specific capacitance of negative electrode (AC),  $\Delta V$  is the potential range of negative electrode during the charge-discharge process, m<sub>+</sub> and m<sub>-</sub> are the mass loading of active material in positive and negative electrodes, respectively.

The specific capacity, energy density and power density of ASCs were calculated from the galvanostatic discharge curves according to the equation 7–9:

Specific capacity:

$$C = \frac{I^* \Delta T}{M} \quad (7)$$

where C is the specific capacity of ASCs (C g<sup>-1</sup>), I is the discharge current (A),  $\Delta T$  is the discharge time (s) and M is the total mass (g) of the active materials in positive and negative electrodes, respectively.

Energy density:

$$E = \frac{I^* \int V dt}{3.6 M} \quad (8)$$

Power density:

$$P = \frac{3600^* E}{\Delta T} \quad (9)$$

where E is the energy density (Wh kg<sup>-1</sup>), I is the discharge current (A), M is the total mass (g) of the active materials in positive and negative electrodes,  $\int V dt$  is the integral area of galvanostatic discharge curves (V s<sup>-1</sup>), P is the power density (W kg<sup>-1</sup>), and  $\Delta T$  is the discharge time (s).

### Acknowledgements

The authors acknowledge the financial support from Natural Science Foundation of Shandong Province (No.

ZR2019MEM036), Major scientific and technological innovation project of Shandong Province (No. 2019JZZY010908), Key Research and Development Program of Shandong Province (No. 2019GGX103006), and Yantai Science and Technology Project (No. 2019XDHZ088).

## Conflict of Interest

The authors declare no conflict of interest.

**Keywords:** electrochemistry · nanoengineering · nanostructures · nickel sulfide · supercapacitors

- [1] J. Jiang, Y. Zhang, P. Nie, G. Xu, M. Shi, J. Wang, Y. Wu, R. Fu, H. Dou, X. Zhang, *Adv. Sust. Syst.* **2018**, *2*, 1700110.
- [2] G. Wang, L. Zhang, J. Zhang, *Chem. Soc. Rev.* **2012**, *41*, 797–828.
- [3] J. Yan, Q. Wang, T. Wei, Z. Fan, *Adv. Energ. Mater.* **2014**, *4*, 1300816.
- [4] C. Liu, F. Li, L. Ma, H. Cheng, *Adv. Mater.* **2010**, *22*, E28–62.
- [5] Y. Wang, Y. Song, Y. Xia, *Chem. Soc. Rev.* **2016**, *45*, 5925–5950.
- [6] R. Kumar, P. Rai, A. Sharma, *J. Mater. Chem. A* **2016**, *4*, 17512–17520.
- [7] M. Salanne, B. Rotenberg, K. Naoi, K. Kaneko, P. L. Taberna, C. P. Grey, B. Dunn, P. Simon, *Nat. Energy* **2016**, *1*, 16070.
- [8] T. Liu, L. Zhang, B. Cheng, J. Yu, *Adv. Energ. Mater.* **2019**, *9*, 1803900.
- [9] F. Beguin, V. Presser, A. Balducci, E. Frackowiak, *Adv. Mater.* **2014**, *26*, 2219–2251.
- [10] M. F. Dupont, S. W. Donne, *J. Power Sources* **2016**, *326*, 613–623.
- [11] J. R. Miller, P. Simon, *Science* **2008**, *321*, 651–652.
- [12] A. González, E. Goikolea, J. A. Barrena, R. Mysyk, *Renewable Sustainable Energy Rev.* **2016**, *58*, 1189–1206.
- [13] P. Simon, Y. Gogotsi, B. Dunn, *Science* **2014**, *343*, 1210–1211.
- [14] Y. Tang, T. Chen, S. Yu, Y. Qiao, S. Mu, S. Zhang, Y. Zhao, L. Hou, W. Huang, F. Gao, *J. Power Sources* **2015**, *295*, 314–322.
- [15] Y. Tang, S. Chen, S. Mu, T. Chen, Y. Qiao, S. Yu, F. Gao, *ACS Appl. Mater. Interfaces* **2016**, *8*, 9721–9732.
- [16] W. Wei, J. Wu, S. Cui, Y. Zhao, W. Chen, L. Mi, *Nanoscale* **2019**, *11*, 6243–6253.
- [17] W. Wei, W. Chen, L. Ding, S. Cui, L. Mi, *Nano Research* **2017**, *10*, 3726–3742.
- [18] T. Li, Y. Zuo, X. Lei, N. Li, J. Liu, H. Han, *J. Mater. Chem. A* **2016**, *4*, 8029–8040.
- [19] H. B. Wu, H. Pang, X. W. Lou, *Energ. Environ. Sci.* **2013**, *6*, 3619.
- [20] Y. Jiang, L. Jiang, Z. Wu, P. Yang, H. Zhang, Z. Pan, L. Hu, *J. Mater. Chem. A* **2018**, *6*, 16308–16315.
- [21] Y. Wang, W. Zhang, X. Guo, K. Jin, Z. Chen, Y. Liu, L. Yin, L. Li, K. Yin, L. Sun, Y. Zhao, *ACS Appl. Mater. Interfaces*, **2019**, *11*, 7946–7953.
- [22] S. Yue, H. Tong, L. Lu, W. Tang, W. Bai, F. Jin, Q. Han, J. He, J. Liu, X. Zhang, *J. Mater. Chem. A* **2017**, *5*, 689–698.
- [23] L. Shen, J. Wang, G. Xu, H. Li, H. Dou, X. Zhang, *Adv. Energ. Mater.*, **2015**, *5*, 1400977.
- [24] Z. Miao, Y. Huang, J. Xin, X. Su, Y. Sang, H. Liu, J. Wang, *ACS Appl. Mater. Interfaces* **2019**, *11*, 18044–18050.
- [25] Q. Wang, J. Yan, Z. Fan, *Energy Environ. Sci.* **2016**, *9*, 729–762.
- [26] X. J. Chen, D. Chen, X. Guo, R. Wang, H. Zhang, *ACS Appl. Mater. Interfaces* **2017**, *9*, 18774–18781.
- [27] X. Han, K. Tao, D. Wang, L. Han, *Nanoscale* **2018**, *10*, 2735–2741.
- [28] X. Shi, H. Wang, S. Ji, V. Linkov, F. Liu, R. Wang, *Chem. Eng. J.* **2019**, *364*, 320–327.
- [29] Z. Yu, Z. Cheng, X. Wang, S. Dou, X. Kong, *J. Mater. Chem. A* **2017**, *5*, 7968–7978.
- [30] Z. Li, X. Li, L. Xiang, X. Xie, X. Li, D. Xiao, J. Shen, W. Lu, L. Lu, S. Liu, *J. Mater. Chem. A* **2016**, *4*, 18335–18341.
- [31] J. Wang, R. Zhou, D. Jin, K. Xie, B. Wei, *Energ. Storage Mater.* **2016**, *2*, 1–7.
- [32] G. Zhang, H. Wu, H. E. Hoster, M. B. Chan-Park, X. Lou, *Energy Environ. Sci.* **2012**, *5*, 9453–9456.
- [33] Y. Huang, T. Shi, S. Jiang, S. Cheng, X. Tao, Y. Zhong, G. Liao, Z. Tang, *Sci. Rep.* **2016**, *6*, 38620.
- [34] X. Yu, X. Lou, *Adv. Energy Mater.* **2017**, *8*, 1701592.
- [35] C. Yuan, H. B. Wu, Y. Xie, X. Lou, *Angew. Chem. Int. Ed. Engl.* **2014**, *53*, 1488–1504.
- [36] B. Yin, Z. Wang, S. Zhang, C. Liu, Q. Ren, K. Ke, *ACS Appl. Mater. Interfaces* **2016**, *8*, 26019–26029.
- [37] C. Lai, M. Lu, L. Chen, *J. Mater. Chem.* **2012**, *22*, 19–30.
- [38] B. You, Y. Sun, *Adv. Energ. Mater.* **2016**, *6*, 1502333.
- [39] W. Li, S. Wang, L. Xin, M. Wu, X. Lou, *J. Mater. Chem. A* **2016**, *4*, 7700–7709.
- [40] A. Ramadoss, K. Kang, H. Ahn, S. I. Kim, S. T. Ryu, J. H. Jang, *J. Mater. Chem. A* **2016**, *4*, 4718–4727.
- [41] T. Wang, B. Zhao, H. Jiang, H. Yang, K. Zhang, M. Yuen, X. Fu, R. Sun, C. Wong, *J. Mater. Chem. A* **2015**, *3*, 23035–23041.
- [42] V. Kalyani, S. Mondal, J. Saha, C. Subramaniam, *Nanoscale* **2018**, *10*, 3663–3672.
- [43] M. Salanne, B. Rotenberg, K. Naoi, K. Kaneko, P. L. Taberna, C. P. Grey, B. Dunn, P. Simon, *Nat. Energy* **2016**, *1*, 16070.
- [44] L. Zuo, W. Fan, Y. Zhang, Y. Huang, W. Gao, T. Liu, *Nanoscale* **2017**, *9*, 4445–4455.
- [45] M. Lu, X. Yuan, X. Guan, G. Wang, *J. Mater. Chem. A* **2017**, *5*, 3621–3627.
- [46] T. Liu, C. Jiang, B. Cheng, W. You, J. Yu, *J. Mater. Chem. A* **2017**, *5*, 21257–21265.
- [47] B. Guan, Y. Li, B. Yin, K. Liu, D. Wang, H. Zhang, C. Cheng, *Chem. Eng. J.* **2017**, *308*, 1165–1173.
- [48] H. Wang, M. Liang, D. Duan, W. Shi, Y. Song, Z. Sun, *Chem. Eng. J.* **2018**, *350*, 523–533.
- [49] C. Dai, P. Chien, J. Lin, S. Chou, W. Wu, P. Li, K. Wu, T. Lin, *ACS Appl. Mater. Interfaces* **2013**, *5*, 12168–12174.
- [50] J. Q. Yang, X. C. Duan, Q. Qin, W. J. Zheng, *J. Mater. Chem. A* **2013**, *1*, 7780–7784.
- [51] Z. Zhang, Z. Huang, L. Ren, Y. Shen, X. Qi, J. Zhong, *Electrochim. Acta* **2014**, *149*, 316–323.
- [52] L. Peng, X. Ji, H. Wan, Y. Ruan, K. Xu, C. Chen, L. Miao, J. Jiang, *Electrochim. Acta* **2015**, *182*, 361–367.
- [53] J. Shao, X. Zhou, Q. Liu, R. Zou, W. Li, J. Yang, J. Hu, *J. Mater. Chem. A* **2015**, *3*, 6168–6176.
- [54] T. Wang, Y. Guo, B. Zhao, S. Yu, H. Yang, D. Lu, X. Fu, R. Sun, C. Wong, *J. Power Sources* **2015**, *286*, 371–379.

Manuscript received: May 11, 2020  
Revised manuscript received: June 5, 2020  
Accepted manuscript online: June 16, 2020  
Version of record online: July 30, 2020